POLITECNICO DI TORINO
Repository ISTITUZIONALE

Graphene layers for ultra-broadband and reconfigurable THz absorption: an analytical model and design procedure

Original
Graphene layers for ultra-broadband and reconfigurable THz absorption: an analytical model and design procedure / Khorshidi, M., Daghighazar, S., Matekovits, L., Ghazizadeh, R.. - In: OPTICS EXPRESS. - ISSN 1094-4087. - ELETTRONICO. - 34:22(2026), pp. 41324-41344. [10.1364/OE.608343]

Availability:
This version is available at: 11583/3016879 since: 2026-10-22T13:01:21Z

Publisher:
Optica Publishing Group

Published
DOI:10.1364/OE.608343

Terms of use:

This article is made available under terms and conditions as specified in the corresponding bibliographic description in the repository

Publisher copyright

(Article begins on next page)

20 November 2026

Research Article Vol. 34, No. 22 / 2 Nov 2026 / Optics Express 41324
Optics EXPRESS

Graphene layers for ultra-broadband and reconfigurable THz absorption: an analytical model and design procedure

MOHAMMADREZA KHORSHIDI,[1,2,5] SHADI DAGHIGHAZAR,[1] LADISLAU MATEKOVITS,[2,3,4,6] AND REZA GHAZIZADEH[1]

[1]Electrical and Computer Engineering Faculty, University of Birjand, 97175/615, Birjand, Iran
[2]Department of Electronics and Telecommunications, Politecnico di Torino, 10129, Turin, Italy
[3]Istituto di Elettronica e di Ingegneria dell'Informazione e delle Telecomunicazioni, National Research Council of Italy, 10129 Turin, Italy
[4]Department of Measurements and Optical Electronics, Politehnica University Timişoara, 300006 Timişoara, Romania
[5]mkhorshidi@birjand.ac.ir
[6]ladislau.matekovits@polito.it

Abstract: An ultra-broadband dual-layer graphene absorber is analyzed and designed using a proposed rigorous analytical model in conjunction with an equivalent circuit model. Based on these models, a systematic design methodology has been developed and validated through the proposed analytical formulation, the equivalent circuit model, and two independent numerical simulation methods, all of which demonstrate excellent agreement. In addition to providing accurate analysis, the proposed analytical model offers deep physical insight into the influence of various design parameters on the performance of graphene-based THz absorbers. The designed absorber achieves greater than 95% uniform absorption over the frequency range of 0.5–2.55 THz, while maintaining absorption above 90% across an overall bandwidth extending from 0.44 to 2.6 THz, corresponding to a normalized bandwidth of 142%. Furthermore, the absorber exhibits exceptional reconfigurability. By tuning the Fermi levels of the graphene layers, the device can be configured to operate over the entire ultra-broadband frequency range, selectively target either the high-frequency or low-frequency region, or function as a broadband reflector. Owing to its moderate fabrication process, tunable response, and versatile operational characteristics, the proposed absorber is highly promising for emerging THz communication and sensing applications.

© 2026 Optica Publishing Group under the terms of the Optica Open Access Publishing Agreement

1. Introduction

The terahertz (THz) frequency range has attracted considerable attention due to its applications in biomedical and imaging [1–3], sensing [4], spectroscopy [5], and high-speed wireless communications. Owing to its short wavelength and non-ionizing nature, THz radiation enables high-resolution and non-destructive operation. However, the development of efficient THz devices, particularly absorbers, remains a major challenge. Since natural materials exhibit weak absorption in the THz regime, engineered periodic structures have been widely investigated to achieve strong and tunable electromagnetic responses [6]. Such absorbers are important for applications including stealth technology [7], radar cross-section reduction [8], electromagnetic interference mitigation [9], and photovoltaics [10]. In particular, subwavelength resonant structures have demonstrated near-unity absorption through engineered electric and magnetic resonances [11]. THz absorbers are generally categorized into metamaterial- and graphene-based structures. Conventional metamaterial absorbers employ metallic resonators with different geometries to realize resonant absorption [12–18]. In contrast, graphene offers several advantages

#608343 https://doi.org/10.1364/OE.608343
Journal © 2026 Received 30 Jul 2026; revised 24 Sep 2026; accepted 29 Sep 2026; published 21 Oct 2026

Optics EXPRESS

for THz and optical applications, including high carrier mobility, tunable conductivity, and strong plasmonic confinement [19]. These properties make graphene highly attractive for tunable and multifunctional THz absorbers and other photonic devices [20]. Decoders, encoders, and optoelectronic half-adder/subtractor circuits based on graphene-nanoshell-coated PhC ring resonators have also been demonstrated, achieving ultra-fast and tunable performance [21–23]. In these devices, silica rods with circular cross-sections coated by a graphene nanoshell form the basic resonator unit, in which electrostatic control of the graphene chemical potential (Fermi energy) via an applied gate voltage governs the transmission path of the incident optical signal through resonator confinement and field enhancement. The electro-optic tunability and high carrier mobility of graphene enable high-speed switching with a wide reconfigurability range in these devices.

Several graphene-based THz absorbers have been proposed to improve absorption bandwidth and tunability [24,25]. However, achieving simultaneously ultrawide bandwidth, high absorption efficiency, and structural simplicity remains challenging. Many reported designs rely on complex multilayer configurations or exhibit limited absorption performance. For instance, Fu et al. [26] proposed a stacked double-layer hexagonal graphene absorber with a TOPAS dielectric, achieving approximately 80% normalized bandwidth with absorption above 90%. A tunable dual-layer graphene ribbon absorber with 118% bandwidth is introduced by Daraei et al. [27], although the absorption remained above only 70%. Wu et al. [28] reported a switchable graphene–vanadium dioxide absorber exhibiting broadband and ultrabroadband modes; however, the use of multiple materials increases fabrication complexity. In another research, Cai et al. [29] developed a three-layer graphene absorber with a relatively narrow bandwidth of about 16%. By using graphene layers combined with dielectric cylinders in [31], they achieved 68% relative bandwidth for absorption above 90%. Similarly, complex multilayer graphene absorbers have also been reported with bandwidths approaching 100% [30].

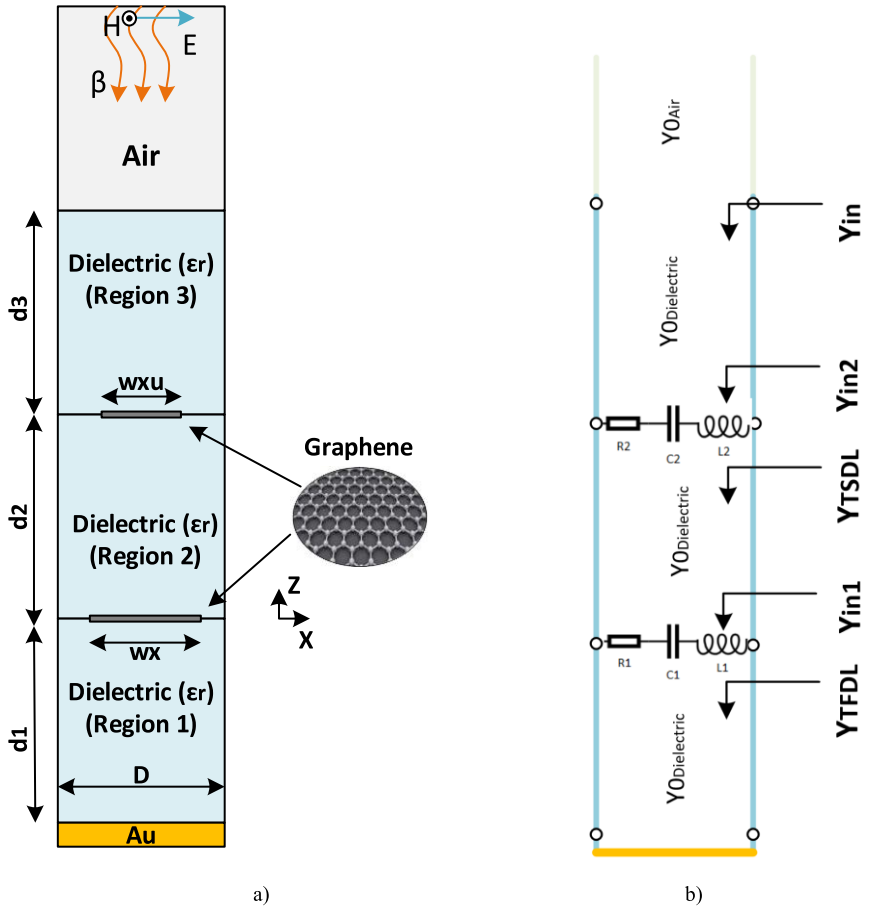
In Ref. [32], we proposed a mode-matching analytical model for the fundamental configuration of a single-layer graphene THz absorber on a dielectric substrate. The single-layer configuration has inherent limitations in simultaneously achieving high absorption and broad bandwidth. To overcome these limitations, this work extends the analytical model to the significantly more complex case of a two-layer graphene absorber, which offers substantially improved absorption performance and bandwidth. A dual-layer graphene THz absorber is proposed and analyzed using a rigorous mode-matching analytical model. Unlike conventional equivalent circuit model (ECM) methods, which rely on approximate formulations, the proposed model provides more rigorous analysis and deeper physical insight into absorber behavior. Using the developed analytical framework together with the ECM, a systematic design methodology is introduced for realizing an ultra-broadband THz absorber with near-unity absorption. In addition, the physical mechanisms and four-state reconfigurable operation of the proposed absorber are investigated.

2. Rigorous analytical model of the two-layer graphene absorber

To develop an analytical model for evaluating the performance of graphene-based THz absorbers, we consider a representative planar structure composed of a periodic array of two-layer graphene ribbons (PAGRs) with periodicity D, width of the lower graphene ribbon wx, placed on a dielectric substrate (Region 1), width of the upper graphene ribbon wxu, embedded between Regions 2 and 3. This configuration serves as a generic model for a broad class of graphene-based THz absorbers and also it has potential to utilize in other devices like comparator and analog-to-digital converter [33,34]. In the proposed structure, the substrate layer (Region 1) and the superstrate layers (Regions 2 and 3) are characterized by the same refractive index, ns, (relative permittivity εr), with corresponding thicknesses d1, d2, and d3, respectively. The entire structure is backed by a metallic ground plane modeled as a perfect electric conductor (PEC), as illustrated in Fig. 1. The absorber is illuminated by a normally incident transverse magnetic (TM)-polarized plane

Optics EXPRESS

wave, where the electric and magnetic field components are oriented along the x- and y-axes, respectively.



a) b)

Fig. 1. a) A unit cell of a two-layer graphene-based THz absorber b) equivalent circuit model of the unit cell.

To analyze the proposed absorber, the mode-matching method is employed. Accordingly, the magnetic field distributions of the electromagnetic wave in the air and dielectric regions can be expressed as follows:

$$H_y^{(i)}(x,z) = \sum_{n=-\infty}^{\infty} (A_n^{(i)} e^{-jK_{z,n}^{(i)} Z} + B_n^{(i)} e^{jK_{z,n}^{(i)} Z}) e^{j\frac{2\pi n}{D}x},\ i = 0,\ 1,\ 2,\ 3 \tag{1}$$

where $H_y{}^{(0)}$, $H_y{}^{(1)}$, $H_y{}^{(2)}$ and $H_y{}^{(3)}$ denote the magnetic fields in air, the substrate layer (region 1) and regions 2 and 3, respectively. The coefficients A_n and B_n represent the modal amplitudes of the incident and reflected electromagnetic waves in each region. $K^{(i)}{}_{Z,n}$ is propagation constant along the z-direction, in region i for $i = 0,1,2,3$ is defined by Eqs. (2) and (3). Since, regions 1, 2, and 3 are composed of the same dielectric material, the corresponding wave numbers in these regions are identical.

$$K_{z,n}^{(0)} = \sqrt{K_0^2 - \left(\frac{2\pi n}{D}\right)^2}, \tag{2}$$

Optics EXPRESS

$$K_{z,n}^{(1)} = \sqrt{K_0^2 \varepsilon_r - \left(\frac{2\pi n}{D}\right)^2} = K_{z,n}^{(2)} = K_{z,n}^{(3)}, \tag{3}$$

Based on Eq. (1) and Maxwell equations, specifically ($\nabla \times \vec{E} = -j\omega\mu \vec{H}$), the electric field can be written as:

$$E_x^{(0)}(x,z) = \frac{1}{j\omega\varepsilon_0} \sum_{n=-\infty}^{n=+\infty} (A_n^{(0)}(-jK_{z,n}^{(0)})e^{-jK_{z,n}^{(0)}z} + B_n^{(0)}(jK_{z,n}^{(0)})e^{jK_{z,n}^{(0)}z})e^{j\frac{2\pi n}{D}x} \tag{4}$$

$$E_x^{(i)}(x,z) = \frac{1}{j\omega\varepsilon_0\ \varepsilon_r} \sum_{n=-\infty}^{n=+\infty} (A_n^{(i)}(-jK_{z,n}^{(i)})e^{-jK_{z,n}^{(i)}z} + B_n^{(i)}(jK_{z,n}^{(i)})e^{jK_{z,n}^{(i)}z})e^{j\frac{2\pi n}{D}x},\ i = 1,2,3 \tag{5}$$

After determining the electric and magnetic fields in the four regions of the proposed structure, the unknown modal coefficients can be obtained by applying the appropriate boundary conditions. In particular, the boundary condition at z = −d1 (corresponding to the PEC ground plane located at the bottom of the substrate), $E_x^{(1)}$(z = -d1) = 0 and Eq. (5) leads to the following relation:

$$B_n^{(1)} = A_n^{(1)} e^{j2K_{z,n}^{(1)}d1} \tag{6}$$

Substituting Eq. (6) into Eqs. (1) and (5), the modal input admittance observed at $z = 0^-$ (immediately below the lower graphene ribbon toward the PEC, at top of the first dielectric layer (TFDL)) can be expressed as:

$$Y_{TFDL,n}(z = 0^-) = \frac{H_{y,n}^{(1)}(z=0)}{E_{x,n}^{(1)}(z=0)} = -\omega\varepsilon_0\ \varepsilon_r \frac{(1 + e^{j2K_{z,n}^{(1)}d1})}{K_{z,n}^{(1)}(1 - e^{j2K_{z,n}^{(1)}d1})} \tag{7}$$

Accordingly, the magnetic field in region (1), i.e., within the substrate layer (region 1), can be rewritten as:

$$H_{y,n}^{(1)}(x, z = 0) = Y_{TFDL,n}(z = 0^-)E_{x,n}^{(1)}(x, z = 0) \tag{8}$$

Similarly, for region 2, by applying Eq. (5) at z = 0 and performing straightforward algebraic manipulations, the coefficient $B_n^{(2)}$ can be obtained as follows:

$$B_n^{(2)} = A_n^{(2)} + \frac{j\omega\varepsilon_0\varepsilon_r}{K_{z,n}^{(2)}} E_{x,n}^{(2)}(x, z = 0) \tag{9}$$

Using Eq. (9) into Eq. (1), the following expression is obtained:

$$H_y^{(2)}(x, z = 0) = \sum_{n=-\infty}^{\infty} \left(2\ A_n^{(2)} + \frac{j\omega\varepsilon_0\varepsilon_r}{K_{z,n}^{(2)}} E_{x,n}^{(2)}(x, z = 0)\right) e^{j\frac{2\pi n}{D}x} \tag{10}$$

Next, the magnetic-field boundary condition is applied at the interface between Regions 1 and 2, where the lower graphene layer is located. The boundary condition at z = 0 is expressed as:

$$H_y^{(2)}(z=0) - H_y^{(1)}(z=0) = \begin{cases} 0, & 0 \le x \le \frac{D-wx}{2}\ and\ \frac{D+wx}{2} \le x \le D \\ \sigma^{(l)}(x) * E_x^{(1)}(z=0), & \frac{D-wx}{2} < x < \frac{D+wx}{2} \end{cases} \tag{11}$$

The right-hand side of Eq. (11) is derived from Ohm's law, J=σ*E, where the symbol * denotes the convolution operator. Substituting Eqs. (8) and (10) into Eq. (11) yields:

$$\left(2\ A_n^{(2)} + \frac{j\omega\varepsilon_0\varepsilon_r}{K_{z,n}^{(2)}} E_{x,n}^{(2)}(x, z = 0)\right) - Y_{TFDL,\,n}(z = 0^-)E_{x,n}^{(1)}(x, z = 0) = \sum_{m=-\infty}^{\infty} \sigma_{n-m}^{(l)}(x) * E_{x,n}^{(1)}(z = 0) \tag{12}$$

It should be noted that the parameters $Y_{TFDL,n}$, and $K_{z,n}$ have already been defined in the previous formulations and are therefore known quantities. The surface conductivity of the lower

Optics EXPRESS

graphene layer, $\sigma^{(l)}$, is determined using the Kubo formula given in Eq. (13), which accounts for both intra-band and inter-band contributions to the graphene conductivity [30].

$$\sigma_{Gr} = \sigma_{intra} + \sigma_{inter} = \frac{2\,k_B T\,e^2}{\pi\,\bar{h}^2}\frac{j}{j\tau^{-1}-\omega}\ln\left[2\cosh\left(\frac{\mathrm{E_F}}{2\,k_B T}\right)\right] - \frac{j\,e^2}{4\pi\,\bar{h}}\ln\left[\frac{2\,\mathrm{E_F} - \bar{h}(\omega - j\tau^{-1})}{2\,\mathrm{E_F} + \bar{h}(\omega - j\tau^{-1})}\right] \tag{13}$$

where $\hbar$ is Planck constant, e is the electron charge, $\mathrm{E_F}$ is the Fermi energy, ω is the angular frequency, τ is the relaxation time. In the THz frequency range, the inter-band contribution can be neglected because $\hbar\omega << 2\mathrm{E_F}$ [26]. Therefore, the graphene surface conductivity is dominated by intra-band transitions, and the corresponding Fourier coefficients of $\sigma^{(l)}$ can be expressed as follows:

$$\sigma_m^{(l)}(\omega) = \frac{\mathrm{E_{F1}}\,e^2}{\pi\,\bar{h}^2}\frac{j}{j\tau^{-1}+\omega}\frac{\mathrm{wx}}{D}\mathrm{Sinc}\left(\frac{m\pi\mathrm{wx}}{D}\right) \tag{14}$$

By substituting Eq. (14) into Eq. (12) we have in matrix form:

$$\begin{bmatrix} \ddots & 0 & 0 & 0 & 0 \\ 0 & Y_{TFDL,-1} & 0 & 0 & 0 \\ 0 & 0 & Y_{TFDL,0} & 0 & 0 \\ 0 & 0 & 0 & Y_{TFDL,1} & 0 \\ 0 & 0 & 0 & 0 & \ddots \end{bmatrix}\begin{bmatrix} \vdots \\ E_{x,-1}^{(1)} \\ E_{x,0}^{(1)} \\ E_{x,1}^{(1)} \\ \vdots \end{bmatrix} - \begin{bmatrix} \ddots & 0 & 0 & 0 & 0 \\ 0 & \frac{\omega\varepsilon_0\varepsilon_r}{K_{z,-1}^{(2)}} & 0 & 0 & 0 \\ 0 & 0 & \frac{\omega\varepsilon_0\varepsilon_r}{K_{z,0}^{(2)}} & 0 & 0 \\ 0 & 0 & 0 & \frac{\omega\varepsilon_0\varepsilon_r}{K_{z,1}^{(2)}} & 0 \\ 0 & 0 & 0 & 0 & \ddots \end{bmatrix}\begin{bmatrix} \vdots \\ E_{x,-1}^{(2)} \\ E_{x,0}^{(2)} \\ E_{x,1}^{(2)} \\ \vdots \end{bmatrix}$$
$$- \begin{pmatrix} \ddots & \sigma_{-1}^{(l)}(\omega) & \sigma_{-2}^{(l)}(\omega) & \sigma_{-3}^{(l)}(\omega) & \sigma_{-4}^{(l)}(\omega) \\ \sigma_1^{(l)}(\omega) & \sigma_0^{(l)}(\omega) & \sigma_{-1}^{(l)}(\omega) & \sigma_{-2}^{(l)}(\omega) & \sigma_{-3}^{(l)}(\omega) \\ \sigma_2^{(l)}(\omega) & \sigma_1^{(l)}(\omega) & \sigma_0^{(l)}(\omega) & \sigma_{-1}^{(l)}(\omega) & \sigma_{-2}^{(l)}(\omega) \\ \sigma_3^{(l)}(\omega) & \sigma_2^{(l)}(\omega) & \sigma_1^{(l)}(\omega) & \sigma_0^{(l)}(\omega) & \sigma_{-1}^{(l)}(\omega) \\ \sigma_4^{(l)}(\omega) & \sigma_3^{(l)}(\omega) & \sigma_2^{(l)}(\omega) & \sigma_1^{(l)}(\omega) & \ddots \end{pmatrix}\begin{bmatrix} \vdots \\ E_{x,-1}^{(1)} \\ E_{x,0}^{(1)} \\ E_{x,1}^{(1)} \\ \vdots \end{bmatrix} = \begin{bmatrix} \vdots \\ 2A_{-1}^{(2)} \\ 2A_0^{(2)} \\ 2A_1^{(2)} \\ \vdots \end{bmatrix} \tag{15}$$

Enforcing the continuity of the tangential electric field component at the interface z = 0 across both regions and applying straightforward algebraic manipulation, the expression for $E_{\mathrm{x,n}}{}^{(2)}$(x, z = 0) is obtained. Further simplification yields the electric field matrix, ***E,*** expressed in terms of the incident mode coefficients $\boldsymbol{A}^{(2)}$, as given in Eq. (16).

$$\boldsymbol{E}^{(2)}(x, z=0) = \boldsymbol{Y}_{\mathrm{in1}}{}^{-1}\;\; 2\,\boldsymbol{A}^{(2)} \tag{16}$$

where, $\boldsymbol{E}^{(2)}$ is an $n \times 1$ matrix with n denoting the number of modes. The square matrix $\mathbf{Y}_{\mathrm{in1}}$ represents the admittance seen from the upper side of the lower graphene layer at $\mathrm{z} = 0^+$ (see Fig. 1(b)), and is composed of the elements $Y_{\mathrm{TFDL},n}$, $\omega\varepsilon_0\varepsilon_{\mathrm{r}}/K^{(2)}{}_{\mathrm{z},n}$ and $\sigma^{(l)}{}_{\mathrm{n}}(\omega)$ after appropriate algebraic simplifications.

Using this result, the admittance top of the second dielectric layer (TSDL), $\mathrm{Y_{TSDL,}}$ observed from $(\mathrm{d2})^-$, i.e., immediately below the upper graphene layer toward the PEC, can be calculated.

$$Y_{TSDL} = Y_0\frac{Y_{\mathrm{in1}} + jY_0\tan(\beta d2)}{Y_0 + jY_{\mathrm{in1}}\tan(\beta d2)} \tag{17}$$

To determine $\mathrm{Y_{in2}}$ at the interface of the upper graphene layer (the boundary between region 2 and 3), the magnetic-field boundary condition at z = d2 is applied. Applying the similar

Optics EXPRESS

boundary-condition procedure used in Eq. (11) yields:

$$\left(2\,A_n^{(3)} + \frac{j\omega\varepsilon_0\varepsilon_r}{K_{z,n}^{(3)}}E_{x,n}^{(3)}(x, z = d2)\right) - Y_{TSDL,n}(z = d2^-)E_{x,n}^{(2)}(x, z = d2) = \sum_{m=-\infty}^{\infty}\sigma_{n-m}^{(u)} * E_{x,n}^{(2)}(z = d2) \tag{18}$$

Equation (18) can be rearranged into the matrix form of Eq. (19), where $\mathbf{Y}_{\text{in2}}$, denotes the admittance observed at z = d2, and $\boldsymbol{A}^{(3)}$ represents the coefficients of the incident wave modes in Region 3.

$$\boldsymbol{E}^{(3)}(x, z = d2) = \boldsymbol{Y}_{\text{in2}}{}^{-1}\;\; 2\,\boldsymbol{A}^{(3)} \tag{19}$$

The admittance $\mathbf{Y}_{\text{in2}}$ consists of the admittance contribution of Region 3, the admittance $\mathbf{Y}_{\text{TSDL}}$, and the modal conductance of the upper graphene layer, as expressed below:

$$\boldsymbol{Y}_{\text{in2}} = j\omega\varepsilon_0\varepsilon_3\boldsymbol{K}_z^{(3)} + \boldsymbol{Y}_{\text{TSDL}} + \boldsymbol{\sigma}^{(u)} \tag{20}$$

Where $\boldsymbol{K}_z{}^{(3)}$ is a diagonal matrix and $\boldsymbol{\sigma}^{(\text{u})}$ is the upper graphene layer conductivity. Having derived $\mathbf{Y}_{\text{in2,}}$ which represents the admittance at z = d2$^+$, the admittance at z = d2 + d3, corresponding to the interface between the dielectric layer in Region 3 and air, can be obtained by transforming $\mathbf{Y}_{\text{in2}}$ to this plane as follows:

$$Y_{\text{in}} = Y_0\frac{Y_{\text{in2}} + jY_0\tan(\beta d3)}{Y_0 + jY_{\text{in2}}\tan(\beta d3)} \tag{21}$$

Subsequently, by substituting this result into an equation analogous to Eq. (16) for the air region, the reflection coefficients, $\boldsymbol{B}^{(0)}$, can be determined. The squared magnitude of $\boldsymbol{B}^{(0)}$ corresponds to the reflected power. Since the structure is backed by a perfect electric conductor (PEC), the transmission coefficient is zero. Consequently, the absorption is equal to 1-$|B_{\text{n}}{}^{(0)}|^2$. It is noted that the total reflectance requires summation over all propagating reflected Floquet orders. It is therefore important to distinguish between propagating and evanescent modes, which is determined by the value of $K^{(i)}{}_{\text{Z,n}}$ in Eqs. (2) and (3): a real value of $K^{(i)}{}_{\text{Z,n}}$ indicates a propagating mode, whereas an imaginary value indicates an evanescent mode.

Up to this point, a rigorous mode-matching analytical model has been developed to evaluate the reflection characteristics of a dual-layer graphene THz absorber. Unlike conventional ECM approaches, the proposed framework captures important design factors often neglected in approximate analyses and provides deeper physical insight into absorber behavior [32]. To validate the model, the results will be compared with those obtained from the ECM and full-wave numerical simulations in the following section.

3. Equivalent circuit model of a two-layer graphene absorber

For assessing the proposed analytical model, the two-layer graphene-based THz absorber, shown in Fig. 1, is analyzed using an ECM. Since the ECM analysis is limited to normally incident waves, the periodic structure can be modeled using transmission-line theory, leading to the equivalent circuit representation shown in Fig. 1(b) [35–37]. Each graphene layer is modeled as a series combination of resistance, inductance, and capacitance elements [38]. These equivalent parameters are determined from the electromagnetic fields and boundary conditions of the periodic graphene ribbon array while incorporating the graphene surface conductivity obtained from the Kubo formula in Eq. (13).

For brevity, several analytical results from Refs. [36,37] are adopted herein, and the reader is referred to these works for detailed derivations. According to Ref. [36], q_n denotes the eigenvalues of the current-distribution equation for a periodic graphene ribbon array and depends on the ratio W/D. Since the operating frequency considered in this work is sufficiently low, only the first mode corresponds to a propagating wave, while higher-order modes are evanescent.

Optics EXPRESS

Therefore, only the dominant mode, q_1, is considered, and its value is determined from Eq. (22) using interpolation of the data reported in Ref. [36].

$$q_1 = -0.3721\pi\frac{wx^2}{D^3} + 0.0467\pi\frac{wx}{D^2} - 0.099\pi\frac{1}{D} + 0.7449\pi\frac{1}{wx} \tag{22}$$

Therefore, as mentioned in Ref. [37]:

$$R = \frac{9D}{8wx}\cdot\frac{\pi\hbar^2}{e^2E_F\tau} \tag{23}$$

$$L = \frac{9D}{8wx}\cdot\frac{\pi\hbar^2}{e^2E_F} \tag{24}$$

$$C = \frac{8wx}{9D}\cdot\frac{2\varepsilon_r}{q_1} \tag{25}$$

Regarding Fig. 1(b), admittance in the TFDL (end of first transmission line and below first graphene layer) can be calculated by:

$$Y_{TFDL} = \left(Y_0\frac{Yau + jY_0\tan(\beta d_1)}{Y_0 + jYau\ \tan(\beta d_1)}\right) \tag{26}$$

which Yau being the Au sheet admittance chosen 10^{12} S. The gold ground plane is modeled as a perfect electric conductor (PEC) in the analytical framework. This approximation is justified by the high reflectivity of gold at THz frequencies (>99.98%) and has been validated by full-wave simulations using the Drude dispersive gold model (ωp=1.37 × 1016 rad/s, α=4.07 × 1013 rad/s), which yield absorption spectra differing from the PEC result by less than 0.15% across the THz operating band. Y_0 is transmission line characteristic admittance and β and d_1 are propagation constant and the substrate thickness, respectively. In order to add graphene effect, graphene admittance is calculated by

$$Y_{\text{lower graphene}} = \frac{1}{R1 + i\omega L1 - \left(\frac{i}{\omega C1}\right)} \tag{27}$$

where R1, L1, and C1 are the equivalent circuit elements of graphene obtained using Eqs. (24)–(26). Therefore, the admittance viewed from the top of the first graphene layer to the metallic back of the absorber as (Y_{in1}) is

$$Y_{in1} = \left(\frac{1}{R1 + i\omega L1 - \left(\frac{i}{\omega C1}\right)}\right) + (Y_{TFDL}) \tag{28}$$

Similarly, the admittance viewed from TSDL (the end of the second transmission line and below the second graphene layer) having thickness d2 and propagation constant β, can be expressed as

$$Y_{TSDL} = Y_0\frac{Y_{in1} + jY_0\tan(\beta d_2)}{Y_0 + jY_{in1}\tan(\beta d_2)} \tag{29}$$

At this stage, the values of the equivalent resistance, inductance, and capacitance of the second graphene layer need to be determined. To this end, Eqs. (23)–(25) can be used, with the understanding that the width wx in these equations should be replaced by the width of the upper graphene ribbon, wxu. As a result, the admittance at the upper graphene layer is:

$$Y_{in2} = \frac{1}{R2 + i\omega L2 - \left(\frac{i}{\omega C2}\right)} + \left(Y_0\frac{Y_{in1} + jY_0\tan(\beta d_2)}{Y_0 + jY_{in1}\tan(\beta d_2)}\right) \tag{30}$$

where R2, L2, and C2 are equivalent resistance, inductance and capacitance of the upper graphene layer. Admittance at the top of the unit cell can be obtained by transforming Y_{in2} through a

Optics EXPRESS

transmission line of length d3. After some mathematical manipulation, the admittance of the entire unit cell is given by:

$$Y_{in} = Y_0 \frac{Y_{in2} + jY_0 \tan(\beta d_3)}{Y_0 + jY_{in2} \tan(\beta d_3)} \tag{31}$$

Finally, reflection coefficient at the interface of a periodic of the unit cell when illuminated by normal incident wave is:

$$\Gamma = \frac{Y_{in} - Y_0}{Y_{in} + Y_0} \tag{32}$$

Consequently, absorption of the unit cell array can be defined by 1-$|\Gamma|^2$.

Using Eqs. (23)–(32) and some complex mathematical manipulations, a closed-form equation has been derived to calculate the electromagnetic absorption of the proposed unit cell array. Although this equation is too lengthy to be presented here, readers can refer to the next section for guidance on designing an optimal absorber.

4. Design procedure and results

The analytical model, proposed in Section 2, is assessed here by comparing results obtained using the ECM, introduced in Section 3 and also by two different numerical methods. For this end, simultaneously a broadband two-graphene layer absorber is designed by a design procedure based on ECM. The following four steps are recommended for applying Eqs. (23)–(32) in the design process:

1- Define the material and structural parameters of the absorber, including the dielectric permittivity, dielectric-layer thicknesses, periodicity, and the center frequency of the desired operating bandwidth for the intended application.

2- Calculate the parameters q_1, R1, L1, C1 for the lower graphene layer using Eqs. (22)–(25), and q_2, R2, L2, C2 for the upper graphene layer, similarly.

3- Parametrically solve Eqs. (22)–(32) to identify suitable ranges for wxu for specific wx, ensuring it provides the desired absorption level and frequency bandwidth.

4- Compute the absorption spectrum and verify the results numerically using simulation packages.

Our goal is applying the above design steps to create an absorber that achieves over 95% absorption of the incident wave across a broad frequency band. As for step 1, periodicity D = 59 μm is selected. Dielectric material is considered with permittivity of 2.25 and low loss tangent, tan $\delta \approx 0.001$, in THz band. The closest real materials to these parameters are TOPAS (cyclic olefin copolymer, COC) with εr=2.35, tan $\delta \approx 0.0006$-0.004 and high-density polyethylene (HDPE) with $\varepsilon r \approx 2.3$, tan $\delta \approx 0.0003$-0.001 at THz frequencies [39]. Since the center frequency of the absorption band is assumed 1.5 THz, the thicknesses of the first and second dielectric layers are set to one-quarter of the wavelength at this frequency, corresponding to 35 μm. (when the wave enters the dielectric layer, reflects off the metallic back plate (considered gold (Au) layer with a conductivity of $\sigma_{Au} = 4 \times 10^7$ [37], acts as a reflective surface to maximize absorption) and returns to the entrance point, its phase shifts to become out of phase with the incident wave, leading to destructive interference and cancellation of the waves). It should be noted that choosing a dielectric thickness of about λ/4 leads to narrow-band performance. However, the presence of two graphene layers with varying widths provides additional design degrees of freedom to achieve a wide frequency bandwidth.

In step 2, the equivalent circuit elements for the graphene layer are calculated. The width of the lower graphene layer is chosen as 55 μm, and the calculated values of the equivalent circuit elements for that are listed in Table 1.

Optics EXPRESS

Table 1. Calculated values of ECM for the lower graphene layer

Parameter	Symbol	Values
Equivalent resistance	R1	129.377 Ω
Equivalent inductance	L1	9.31*10^(-12) H
Equivalent capacitance	C1	1.47*10^(-15) F

In the third step of the design process, the material and geometric parameters defined in step one, along with those calculated in step two, are substituted into the key Eqs. (22) and (32), and the equations are solved parametrically. Due to the complexity of the resulting expression, it is not presented explicitly. Instead, its behavior for different parameter values is illustrated graphically. After mathematical simplification, the parameter range corresponding to absorption above 95% is shown in Fig. 2.

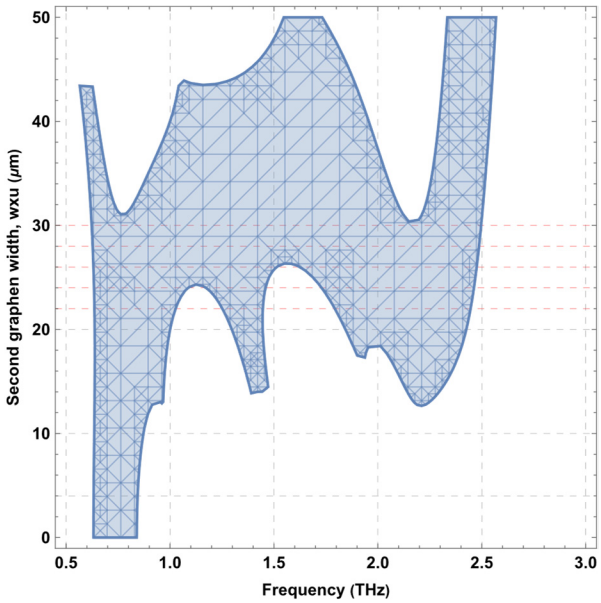


Fig. 2. Absorption spectra for different values of the upper graphene ribbon width, wxu when absorption set above 95% and wx = 55 μm (The hatched region indicates values of wxu for which absorption exceeds 95%. To aid readability, the range 20–30 μm is delineated by dashed red lines with a step size corresponding to the parameter increment.).

The vertical axis of Fig. 2 represents different values of wxu, while the horizontal axis corresponds to frequency. Figure 2 illustrates the suitable values for the width of the upper graphene ribbon, wxu, when the absorption threshold is set to 0.95. If wxu is chosen within the hatched region, the absorption will consistently exceed 95%. As inferred from Fig. 2, selecting wxu=29 μm is expected to yield the maximum frequency bandwidth with continuous absorption performance above 95%. As shown in Fig. 2, the proposed absorber demonstrates stable absorption performance with respect to variations in the upper ribbon width wxu, tolerating a fabrication deviation of approximately ±10% over the range 26–32 μm. The sensitivity of the absorption performance to the remaining structural parameters is further investigated in Fig. 5. The absorber's performance is re-optimized by making minor adjustments to the thicknesses of the dielectric layers in order to maximize the attainable bandwidth. An absorber with deliberately

Optics EXPRESS

chosen parameters (listed in Table 2) is analyzed, and its calculated absorption performance is shown in Fig. 3.

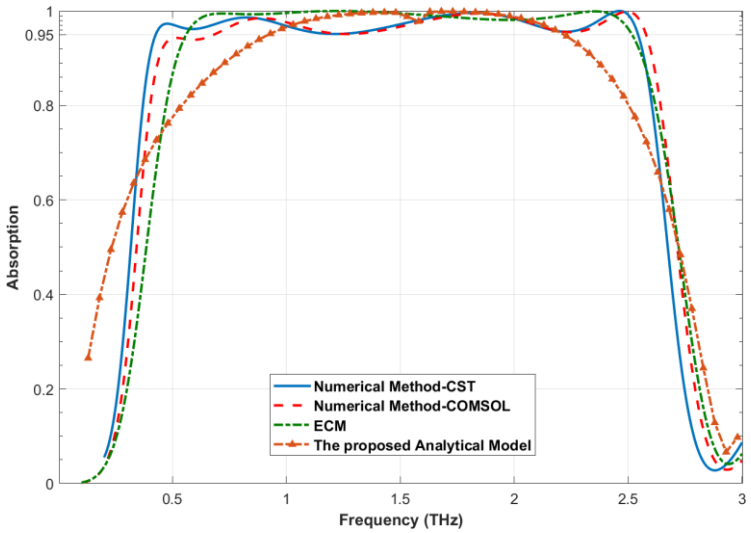


Fig. 3. Absorption spectra of the proposed absorber calculated by the proposed analytical model, ECM, COMSOL, and CST simulations (wx = 55 μm, wxu = 29 μm, D = 59 μm, E_{F1} = 1.1, E_{F2} = 0.6, d1 = 35 μm, d2 = 32 μm and d3 = 33 μm).

Table 2. Selected parameters of the absorber and calculated values by ECM

Parameter	Symbol	Values
Periodicity	D	59 μm
Width of the lower graphene ribbon	wx	55 μm
Width of the upper graphene ribbon	wxu	29 μm
Thickness of the first dielectric layer	d1	35 μm
Thickness of the second dielectric layer	d2	32 μm
Thickness of the third dielectric layer	d3	33 μm
Equivalent resistance of second graphene layer	R2	449.8 Ω
Equivalent inductance of second graphene layer	L2	3.23*10^(-11) H
Equivalent capacitance of second graphene layer	C2	2.42*10^(-16) F
Graphene and Dielectric parameters		
Fermi energy of lower / upper graphene ribbon	E_{F1} / E_{F2}	1.1 / 0.6 eV
Relaxation time for lower / upper graphene ribbon	τ1 / τ2	1.1×10^{-13} / 0.6×10^{-13} S
Electron mobility	μ	0.1 m^2/Vs (1000 cm^2/Vs) [20]
graphene Fermi velocity	vF	10^6 m/s [37]
Temperature	T	300 K
Dielectric loss tangent	tan δ	0.0006
Gold conductivity and thickness	σ_{Au}	4×10^7 S/m [37]
Graphene thickness	-	1 nm
Gold thickness	-	300 nm

Optics EXPRESS

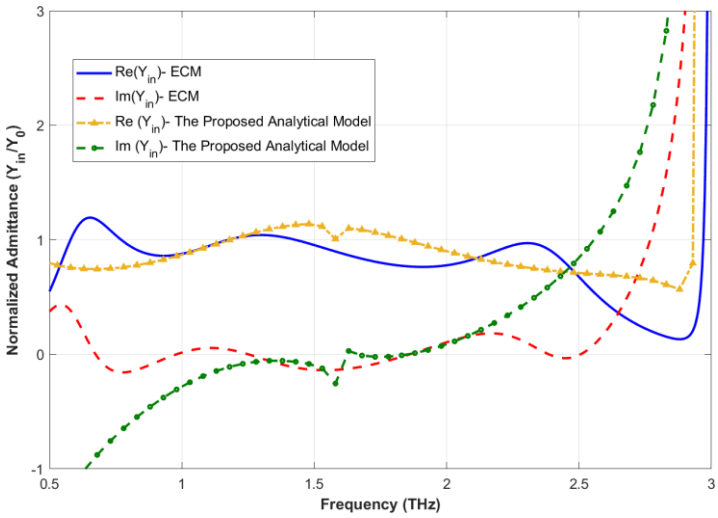
The absorber is simulated using two different electromagnetic software packages: COMSOL Multiphysics and CST Studio Suite. As noted in Section 2, only propagating modes contribute to the reflectance calculation in the mode-matching method. The propagation criterion depends on both the periodicity and the permittivity of the surrounding medium. By selecting D = 59 μm, only the zero-order Floquet mode propagates for frequencies below 3 THz. Consequently, only the zero-order mode is retained in the mode-matching formulation for the calculation of reflectance and absorption.

As shown in Fig. 3, the results from both the proposed analytical model and ECM exhibit excellent agreement with that of obtained by numerical simulations. The largest discrepancy between the analytical and numerical results occurs at the lower and upper edges of the absorption band, where absorption exceeds 95%. At 0.5 THz and 2.5 THz, the maximum absolute error is approximately 0.15 (15%), which is considered acceptable for the proposed analytical model. This confirms the validity and accuracy of the proposed analytical model. It is noted that designing an optimal absorber using these numerous design parameters without the proposed design procedure requires many extensive numerical simulations. For reference, a single frequency-domain simulation of the full structure with all parameters fixed requires approximately 220 seconds in COMSOL (2D, frequency-domain solver, 13,385 triangular mesh elements, relative tolerance=0.01) and approximately 3 minutes in CST Microwave Studio (3D, frequency-domain solver, 247,100 tetrahedral mesh elements) on a system equipped with an Intel Core i7 processor and 16 GB of RAM. Therefore, the proposed design procedure using analytical models provides a direct path to near-optimal values for these many design parameters.

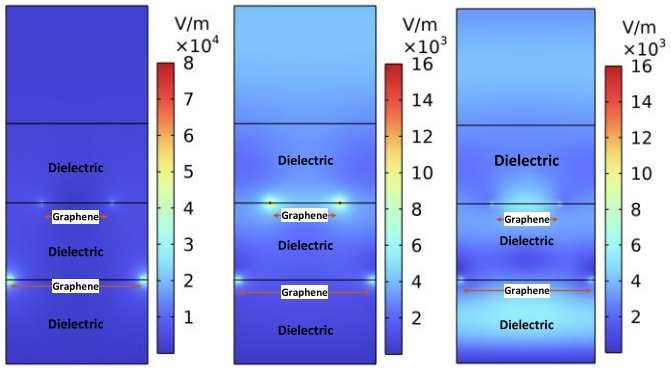
The designed THz absorber achieves over 95% absorption of the incident wave across a broad frequency range from 0.5 THz to 2.55 THz, with a uniform absorption performance. For absorption levels above 90%, the absorber covers a frequency range from 0.44 THz to 2.6 THz (corresponding to a normalized bandwidth of 142%) which, to the best of the authors' knowledge, is the highest reported thus far. This high level of absorption, combined with its wide bandwidth, bestows the absorber with a unique feature that sets it apart from others. The broadband absorption originates from the combined effects of impedance matching (as shown in Fig. 4(a)), localized plasmonic resonances in the graphene ribbons (as shown in Fig. 4(b,c,d,e,f)), and multiple Fabry–Pérot-like cavity resonances within the dielectric layers (as shown in Fig. 4(b,c,d)). Figures 4(e) and 4(f) show the electric field magnitude distribution along the lower and upper graphene ribbon layers, respectively, evaluated in the x-direction at representative frequencies. In both figures, the electric field intensity is sharply concentrated at the ribbon edges, which is the characteristic signature of localized ribbon plasmon resonance excitation. These mechanisms suppress reflection over a wide frequency range and enhance electromagnetic energy confinement inside the structure.

To assess the sensitivity of the proposed absorber's design, the effects of varying the width of the graphene ribbons are shown in Fig. 5. As illustrated, the absorber demonstrates good robustness against fluctuations in the graphene widths, indicating that small variations during the fabrication process will not significantly affect its performance. As shown in Fig. 5(c), selecting a first dielectric layer thickness of 35 μm yields the maximum achievable frequency bandwidth with absorption exceeding 95%. The second dielectric layer thickness is a more sensitive parameter: as shown in Fig. 5(d), any deviation from 32 μm reduces the absorption from above 95% to above 90% across a portion of the operating bandwidth. Figure 5(e) evaluates the effect of a uniform variation in the dielectric permittivity on the absorption performance. Increasing εr from 2.1 to approximately 2.4 narrows the frequency bandwidth over which absorption exceeds 95%, with the degradation occurring at the upper edge of the band. It is therefore concluded that the second dielectric layer thickness is the most fabrication-sensitive structural parameter of the proposed absorber.

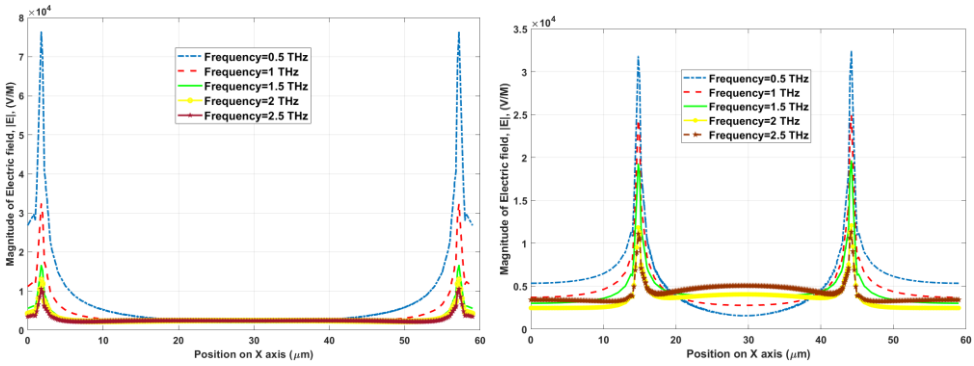
Optics EXPRESS



a)



b) c) d)



e) f)

Fig. 4. Two main reasons underlie the wide, high absorption performance of the designed absorber a) Real and imaginary parts of the normalized input admittance spectrum calculated using the ECM, and the proposed analytical model b) Electric field distributions, $|\mathbf{E}|$, obtained from numerical simulations at frequencies of 0.5 THz, c) 1.5 THz, and d) 2.5 THz (e) Electric field magnitude distribution along the lower graphene ribbon layer. (f) Electric field magnitude distribution along the upper graphene ribbon layer.

Optics EXPRESS

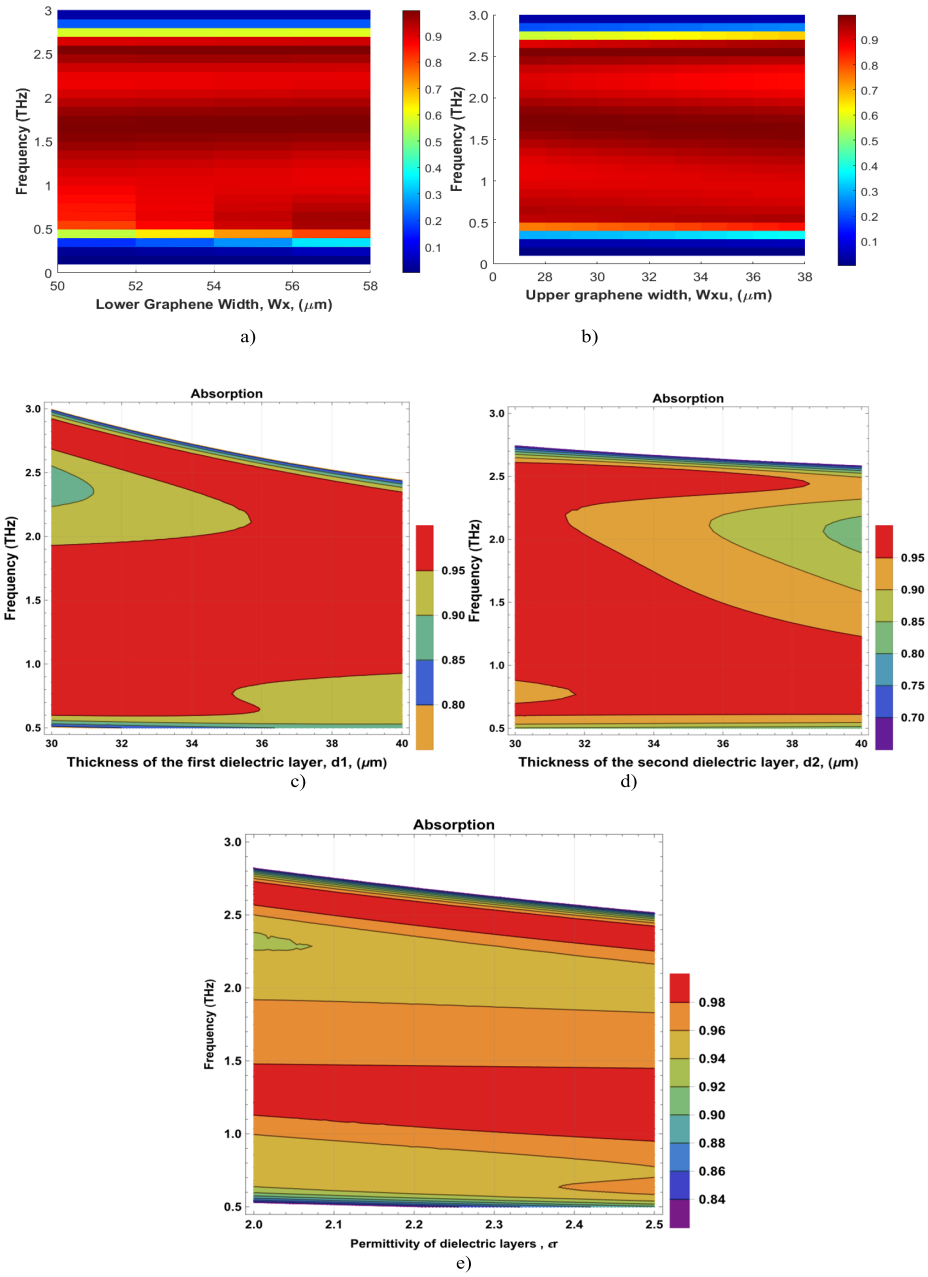


Fig. 5. Absorption versus frequency and variations of a) width of the lower graphene ribbon when wxu = 29 µm b) width of the upper graphene ribbon when wx = 55 µm. c) thickness of first dielectric layer, d1 when d2 = 32 µm and d3 = 33 µm d) thickness of second dielectric layer, d2 when d1 = 35 µm and d3 = 33 µm) dielectric permittivity εr of dielectric layers, with all other parameters fixed at the nominal values listed in Table 2.

As shown in Fig. 6, the proposed absorber maintains ultra-broadband absorption performance for angles of incidence ranging from 0° to 70°. As the angle of incidence increases, the absorption band shifts slightly toward higher frequencies while the bandwidth is substantially preserved.

Optics EXPRESS

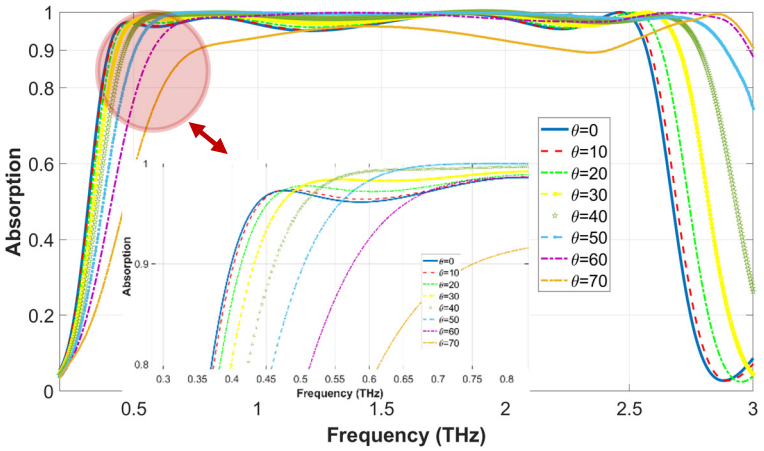


Fig. 6. Absorption versus various angles of incident wave and frequency obtained by COMSOL, wx = 55 μm, wxu = 29 μm.

The proposed absorber with one-dimensional graphene ribbon arrays oriented along the y-direction is inherently polarization-sensitive. Under TM polarization (electric field perpendicular to the ribbon axis), the ribbon plasmon resonance is efficiently excited, producing broadband absorption exceeding 90% over 0.44–2.6 THz at normal incidence. Under TE polarization (electric field parallel to the ribbon axis), the plasmon resonance along the ribbon width direction is not excited, and the absorption response will be degraded. Consequently, the structure is not polarization-insensitive, and its high absorption performance is restricted to TM polarization. To achieve polarization-insensitive operation, a two-dimensional symmetric geometry, such as crossed ribbon arrays, square patch arrays, or rotationally symmetric disc/ring patterns would need to be introduced, at the cost of additional fabrication complexity.

5. Multifunctional reconfigurability of the proposed absorber

The analytical approach provides us with the ability to predict the absorber's performance across different configurations. In this section, we demonstrate the application of the proposed absorber as a reconfigurable device, capable of operating in various states. By adjusting the Fermi levels of the graphene ribbons (gating or chemical doping) specifically E_{F1} and E_{F2}, the parameters R1, C1, L1, R2, C2, L2, calculated using Eqs. (22)–(25), can be tuned accordingly. It is noted that the relaxation time (τ) is intrinsically linked to the Fermi level via the relationship $\tau = \mu E_F / (e\ vF^2)$, where μ is electron mobility and $vF = 10^6$ m/s is the graphene Fermi velocity [37]. A change in E_F alters the carrier density, which in turn affects τ. These modifications result in change in the absorption frequency bands of the structure.

To identify the optimal Fermi level values, the proposed design procedure is repeated for different E_{F1}, E_{F2}, and frequency ranges. Four distinct configurations of the absorber are defined, as summarized in Table 3.

It is noted that $E_F = 0$ is not physically realizable in practice. The simplified intraband model becomes invalid at the Dirac point ($E_F = 0$) for three principal reasons. First, the condition $\hbar\omega << 2E_F$ is violated at $E_F = 0$, so interband transitions cannot be neglected. Second, the relaxation-time expression $\tau = \mu E_F / (e\ vF^2)$ predicts τ approaches zero as E_F approaches zero, which is physically unrealistic since residual disorder and charge-puddle effects produce a finite minimum scattering rate. Third, at T = 300 K, thermal excitation generates a finite intrinsic carrier density of $(\pi/6)(K_B T/\hbar\ vF)^2 = 8.1 \times 10^{10}\ cm^{-2}$ [40,41] even at $E_F = 0$, corresponding to an effective thermal Fermi energy of approximately 33 mV. In realistic graphene samples,

Optics EXPRESS

Table 3. Four states that enable the proposed absorber to operate

State number	states	E_{F1} [eV]	E_{F2} [eV]
1	Ultra-broadband absorber	1.1	0.6
2	High-frequency absorber	0.05	1.2
3	Low-frequency Absorber	0.8	1.2
4	Reflector	0.05	0.05

charge puddles further increase the residual carrier density to approximately 10^{11}–$10^{12}\,cm^{-2}$. Consequently, the conductivity at $E_F = 0$ is finite and cannot be accurately described by the simplified intraband model [42]; a full finite-temperature Kubo formulation retaining both intraband and interband contributions is required near the Dirac point. For the reconfigurability assessment, a minimum Fermi energy of $E_F = 0.05$ eV is therefore adopted as a physically safe lower bound, with the relaxation time set accordingly to τ=10 fs.

State 1 has been explained in detail in the previous section. In this state, the absorber functions as an ultra-broadband absorber with a uniform absorption greater than 95%.

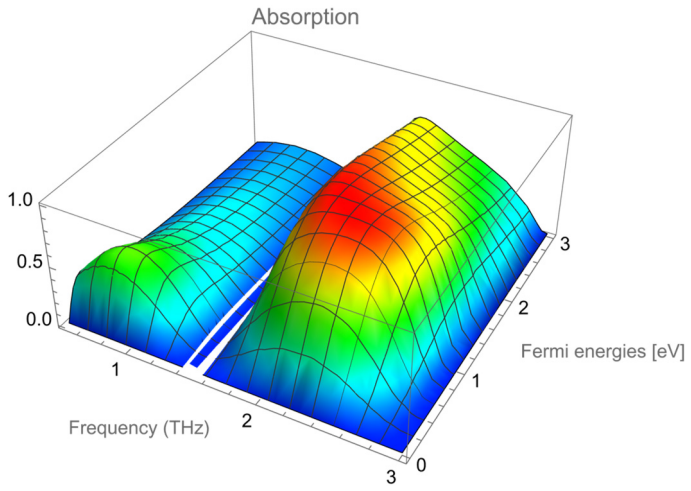
For applications requiring absorption primarily at the higher-frequency end, the Fermi levels are set to $E_{F1} = 0.05$ and $E_{F2} = 1.2$ eV, resulting in strong absorption over the 1.85–2.57 THz range. The optimal Fermi levels are determined using the analytical model presented in Section 2 and 3 and verified through numerical simulations. As shown in Fig. 7, increasing E_{F2} shifts the absorption toward higher frequencies while reducing absorption at the lower end of the band.

In the third operating state, setting $E_{F1} = 0.8$ eV and $E_{F2} = 1.2$ eV shifts the absorption band toward lower frequencies, yielding narrowband operation over approximately 0.45–0.9 THz, as shown in Fig. 8. Since all structural parameters remain unchanged between states 2 and 3 with the exception of E_{F1}, any difference in absorption performance relative to state 2 originates exclusively from the change in E_{F1}. The Fabry–Pérot-like cavity absorption is inherently present in both states. Consequently, the change in low-frequency absorption relative to state 2 can be attributed to the shift in plasmon resonance frequency, which scales as $\omega p \propto \sqrt{EF}$ [43,44]: increasing the Fermi energy of the lower graphene layer from 0.05 eV in state 2 to 0.8 eV in state 3 shifts its plasmonic resonance from well below the operating bandwidth to near the lower edge of the band. This shift results in the observed increase in low-frequency absorption relative to state 2, as illustrated in Fig. 8. In a narrow frequency range around 2.8 THz, the absorption reaches approximately 90%. However, this does not affect the performance of the designed absorber, as this frequency range lies outside its operating bandwidth.

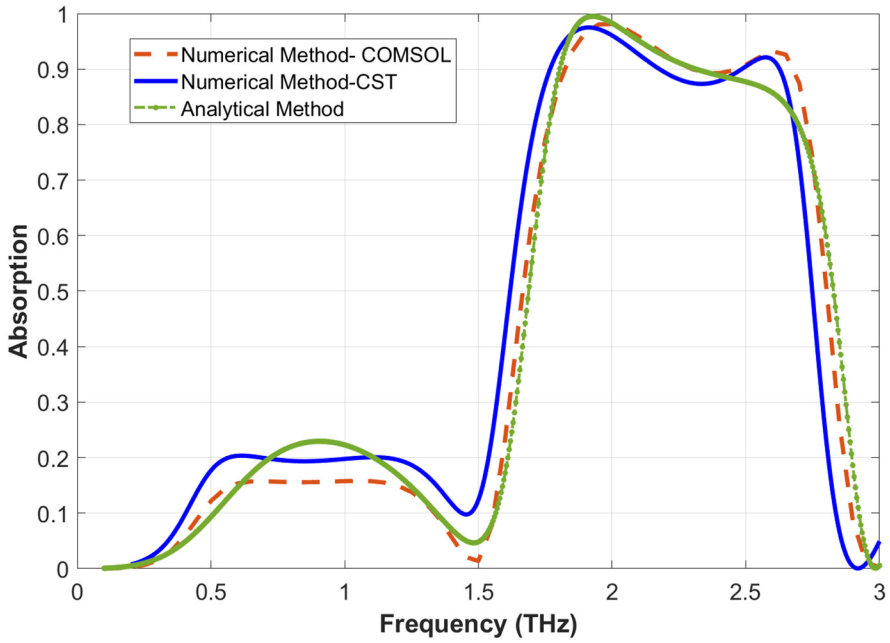
When both Fermi levels are set to 0.05 eV, the structure operates as a reflector, with only about 5% absorption across the considered frequency range, as illustrated in Fig. 9.

From an implementation perspective, two independent configurations can be considered for the practical fabrication of the proposed structure: an independently gated configuration and an ion-gel-based configuration. In the first configuration, the two graphene ribbon layers are separated by a dielectric spacer, and each layer is independently gated. The upper graphene layer is controlled by a top gate electrode, while the lower graphene layer is controlled by a bottom gate electrode. Both gate electrodes share the metallic ground plane as a common electrode. An independent DC bias source is applied to each gate, allowing the Fermi level of each graphene layer to be individually tuned without significant electrical cross-coupling [45]. The relevant time scale of the proposed absorber is the response time of the gate-voltage-controlled Fermi energy, which is set by the RC time constant of the graphene–dielectric–metal stack where the coefficient $\varepsilon_0 \varepsilon r/ed$ in Eq. (33) is called gate capacitance [23]. Since the proposed absorber does not operate as a switch and its response time is typically in the nanosecond range for electrostatic gating, the absorber has suitable performance regarding response time.

Optics EXPRESS



a)

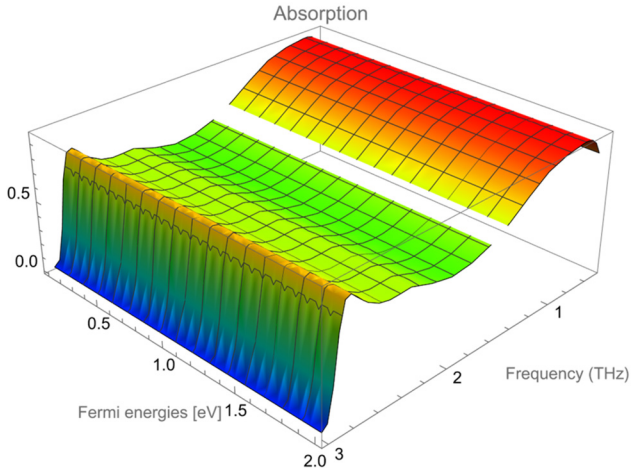


b)

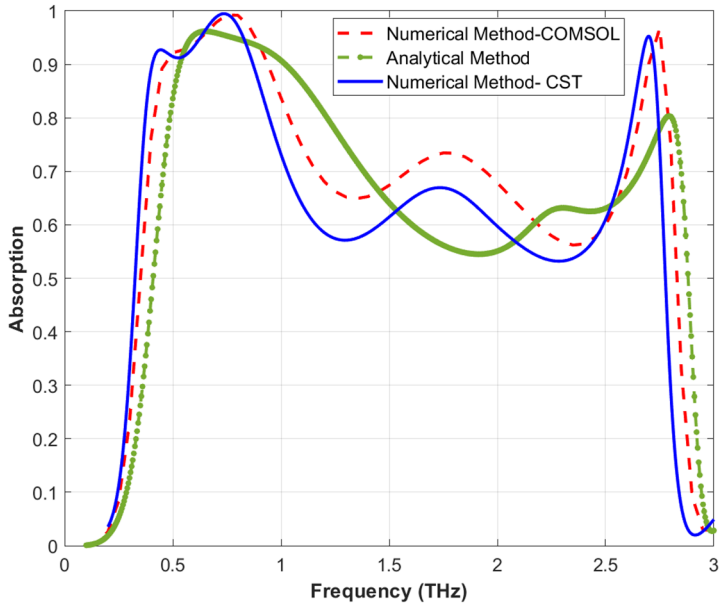
Fig. 7. a) 3D view of absorption versus frequency and E_{F2} when $E_{F1} = 0.05$ b) Absorption of the designed absorber when its Fermi energies are set as $E_{F1} = 0.05$, $F_{E2} = 1.2$ [eV]

Alternatively, two ion-gel layers ($\varepsilon r = 2.56$) can be individually coated onto the two graphene layers and used as gate dielectrics. An ion-gel is a gel-like material composed of an ionic liquid immobilized within a polymer matrix. Owing to their gel-like nature, ion-gels can be directly spin-coated onto graphene as thin, uniform layers. Their high ionic conductivity and optical transparency enable independent gate voltages to be applied to each graphene layer, and their 10 nm thickness has a negligible effect (obtained by our simulation: lower than 0.01%) on the absorption performance of the structure [46].

Optics EXPRESS



a)



b)

Fig. 8. a) 3D view of absorption versus frequency and E_{F2} when $E_{F1} = 0.8$ b) absorption of the designed absorber when its Fermi energies are set as $E_{F1} = 0.8$, $F_{E2} = 1.2$ [eV]

The gating mechanism relies on the formation of an electrical double layer (EDL). When a gate voltage Vg is applied, mobile ions in the ion-gel redistribute, accumulating at both the metal/ion-gel and ion-gel/graphene interfaces. At the latter, counter-ions pack directly against the graphene surface to a thickness of approximately 0.3–1 nm, roughly the diameter of one ion. The resulting dense ionic charge sheet electrostatically induces an equal and opposite carrier sheet in graphene. The EDL therefore behaves as a parallel-plate capacitor with an exceptionally

Optics EXPRESS

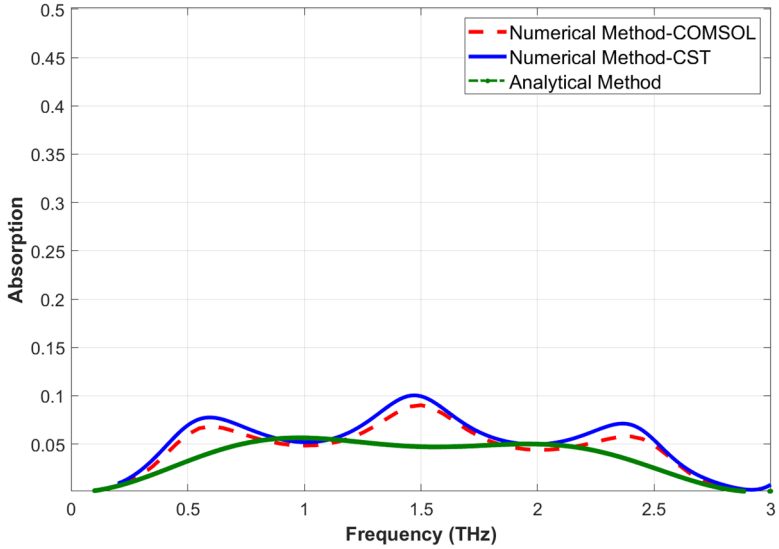


Fig. 9. Absorption of the designed absorber when its Fermi levels are set as $E_{F1} = 0.05$, $F_{E2} = 0.05$ [eV]

small effective separation $d_{EDL} = 0.3$–1 nm, giving an areal capacitance:

$$C_{EDL} = \frac{\varepsilon_0 \varepsilon_{rlocal}}{d_{EDL}} \tag{33}$$

where $\varepsilon_{rlocal} = 5$–10 is the local permittivity of the ionic liquid near the interface. For representative values $\varepsilon_{rlocal} = 7$ and $d_{EDL} = 0.5$ nm, this gives C_{EDL}=12.4 μF/cm^2, which is three to four orders of magnitude larger than that of a conventional 10 nm dielectric layer with εr = 2.56. Experimentally measured values for ion-gel/graphene systems range from 10 to 40 μF/cm^2 [47].

$$n = \frac{1}{\pi}\left(\frac{E_F}{\hbar v_F}\right)^2 \tag{34}$$

Using Eq. (34), the carrier densities, n, corresponding to $E_{F1} = 1.1$ eV and $E_{F2} = 1.2$ eV are 8.89×10^{13} cm^{-2} and 1.06×10^{14} cm^{-2}, respectively.

$$V_g = \frac{n\, e}{C_{EDL}} \tag{35}$$

Substituting into Eq. (35) with C_{EDL} in the range 10–40 μF/cm^2, the required gate voltages are 0.71–1.42 V for E_{F1} and 0.85–1.69 V for E_{F2}, both well within the typical electrochemical stability window of ion-gel systems (3–5 V) [48,49], confirming that the required Fermi-level tuning is achievable without risk of electrochemical degradation.

Regarding interlayer electrical isolation, the two graphene layers are separated by dielectric region 2 of thickness $d2 > 30$ μm. The mutual capacitance per unit area between them is $\varepsilon_0 \varepsilon r / d2 = 62$ pF/cm^2. This is less than 1% of the self-gate capacitance 10–40 μF/cm^2, so capacitive cross-coupling between the two independently gated layers is negligible.

Overall, by tuning the graphene Fermi levels, the proposed structure can operate as an ultra-broadband absorber, a high-frequency absorber, a low-frequency narrowband absorber, or a reflector, demonstrating excellent reconfigurability for adaptive THz applications.

The proposed THz absorber is compared with recent graphene-based THz absorbers of notable performance reported in the literature, and the results are summarized in Table 4. As can be seen,

Optics EXPRESS

the proposed absorber achieves the highest fractional bandwidth among all surveyed designs while maintaining absorption exceeding 95% across a broad continuous frequency range. Furthermore, the key differentiator of the proposed work is the combination of an analytical mode-matching model, an equivalent circuit model, and a systematic design procedure with fabrication tolerance verification, a combination that, to the best of the authors' knowledge, has not been reported in any of the related references.

Table 4. Comparison of graphene-based broadband THz absorbers

Ref.	No. of Graphene Layers	Absorption Threshold (%)	Freq. Range (THz)	FBW (%)	Tunability	Validation Method	Total Dielectric Thickness d (μm)	$d / \lambda_g = d\sqrt{\varepsilon_r} / \lambda_0$
[50]	1 (hybrid sq/disk/loop) (TOPAS; $\varepsilon_r = 2.35$)	>90	1.38–3.40	84.5	Yes (EF)	Numerical (FDTD)	~12	0.147
[51]	1 (SiO2; $\varepsilon_r = 3.9$)	>90	~0.5–2.5	131	Yes (EF)	Analytical + Numerical	~25	0.247
[52]	1 (circular patch) (SiO2; $\varepsilon_r = 3.9$)	>90	1.0–3.0	~100	Yes (EF)	Numerical (FDTD)	~25	0.329
[53]	1 (patterned) (TOPAS; $\varepsilon_r = 2.35$)	>90	3.31–7.15	73.4	Yes (EF)	Numerical (FDTD)	~7	0.187
[54]	1 (strip/ribbon) (Polyimide; $\varepsilon_r = 3.5$)	>90	~2.0–6.0	105	Yes (EF)	Numerical	~10	0.249
[55]	1 (disk/cross ring) (SiO2; $\varepsilon_r = 3.9$)	>90	0.6–1.75 & 3.25–4.08	98.3/22.7 (dual)	Yes (EF)	Numerical (CST) + Equiv. circuit	~40	0.309
[56]	1 (rect. ring + crossbars) (SiO2; $\varepsilon_r = 3.9$)	>90	~2.0–5.0	~85	Yes (EF)	Numerical (FDTD)	~12	0.277
[57]	1 (disk array) (SiO2; $\varepsilon_r = 3.9$)	>90	~1-2.5	~85	Yes (EF)	Numerical (CST)	~25	0.329
[58]	1 (Multi-layer polyimide + silicon $\varepsilon_r \sim 9.0$)	>90	2.56–11.6	~127	Yes	Numerical	~2.5	0.17
Proposed work	**2 (ribbon array) (Dielectric; $\varepsilon_r = 2.25$)**	**>90 (>95)**	**0.44–2.6 (0.5-2.55)**	**142 (134)**	**Yes (EF)**	**Analytical (Mode Matching Method) + Numerical**	**100**	**0.75**

6. Conclusion

Highly absorptive devices with broad operating bandwidths are essential for a wide range of emerging THz technologies. To address this demand, a two-layer graphene-based THz absorber was rigorously analyzed using the proposed analytical model based on mode-matching method. The proposed configuration gives rise to a coupled system of two Fabry–Pérot resonators with closely spaced resonant frequencies which, in conjunction with the localized plasmonic resonances of the graphene ribbons, significantly enhancing the operational bandwidth of the absorber. Based on the analytical framework, a systematic design procedure for wideband graphene-based THz absorbers was developed. The performance of the proposed absorber, together with the

Optics EXPRESS

analytically predicted results, was validated using an equivalent circuit model and two independent numerical simulation methods. The designed absorber achieves absorption greater than 95% over the broad frequency range of 0.5–2.55 THz. Furthermore, the absorption bandwidth for absorption levels exceeding 90% extends from 0.44 to 2.6 THz, corresponding to a normalized bandwidth of 142%. In addition, the absorber demonstrates remarkable reconfigurability. By simply tuning the Fermi levels of the graphene layers, the device can selectively operate in either the higher-frequency band (1.85–2.57 THz) or the lower-frequency band (0.45–0.9 THz), or alternatively function as a broadband reflector across the entire frequency range.

Disclosures. The authors declare no conflicts of interest.

Data availability. The data that support the findings of this study are available within the article.

References

1. L. Tan, D. Wang, and K. D. Xu, "Terahertz metamaterials for spectrum modulation: structural design, materials and applications," Mater. Des. **244**, 113217 (2024).
2. M. Abdollahvand, M. Khorshidi, S. Sobhi-Givi, *et al.*, "An innovative in-body adjustable triple-band Notch UWB monopole antenna with improved bandwidth performance," Sci. Rep. **15**(1), 24538 (2025).
3. K. Aliqab, A. Armghan, and M. Alsharari, "Polarization insensitive and wideband terahertz absorber using high-impedance resistive material of RuO2," Sci. Rep. **14**(1), 19149 (2024).
4. M. S. Islam, J. Sultana, M. Biabanifard, *et al.*, "Tunable localized surface plasmon graphene metasurface for multiband superabsorption and terahertz sensing," Carbon **158**, 559–567 (2020).
5. S. L. Dexheimer, ed., *Terahertz spectroscopy: principles and applications*, (CRC press, 2017).
6. H. T. Chen, J. F. O'Hara, A. J. Taylor, *et al.*, "Complementary planar terahertz metamaterials," Opt. Express **15**(3), 1084–1095 (2007).
7. K. Iwaszczuk, A. C. Strikwerda, K. Fan, *et al.*, "Flexible metamaterial absorbers for stealth applications at terahertz frequencies," Opt. Express **20**(1), 635–643 (2012).
8. S. Genovesi, F. Costa, and A. Monorchio, "Low-profile array with reduced radar cross section by using hybrid frequency selective surfaces," IEEE Trans. Antenn. Propag. **60**(5), 2327–2335 (2012).
9. Y. Zhang, H. Dong, N. Mou, *et al.*, "High-performance broadband electromagnetic interference shielding optical window based on a metamaterial absorber," Opt. Express **28**(18), 26836–26849 (2020).
10. R. M. H. Bilal, M. A. Baqir, M. Hameed, *et al.*, "Triangular metallic ring-shaped broadband polarization insensitive and wide-angle metamaterial absorber for visible regime," J. Opt. Soc. Am. A **39**(1), 136–142 (2022).
11. M. Khorshidi, S. Zafari, and G. Dadashzadeh, "Increase in terahertz radiation power of plasmonic photoconductive antennas by embedding buried three-stepped rods in electrodes," Opt. Express **27**(16), 22327–22338 (2019).
12. D. Chen, B. Xu, Z. Qiu, *et al.*, "Ultra-broadband terahertz metamaterial absorber based on flexible wave-absorbing material," Results Phys. **52**, 106880 (2023).
13. G. Labate, A. Alù, and L. Matekovits, "Surface-admittance equivalence principle for nonradiating and cloaking problems," Phys. Rev. A **95**(6), 063841 (2017).
14. Z. Hamzavi-Zarghani, A. Yahaghi, L. Matekovits, *et al.*, "Tunable mantle cloaking utilizing graphene metasurface for terahertz sensing applications," Opt. Express **27**(24), 34824–34837 (2019).
15. S. Li, L. Zhang, and X. Chen, "3D-printed terahertz metamaterial absorber based on vertical split-ring resonator," J. Appl. Phys. **130**(3), 3 (2021).
16. Z. Hamzavi-Zarghani, A. Yahaghi, and L. Matekovits, "Reconfigurable metasurface lens based on graphene split ring resonators using Pancharatnam–Berry phase manipulation," Journal of Electromagnetic Waves and Applications **33**(5), 572–583 (2019).
17. H. Zhu, Y. Zhang, L. Ye, *et al.*, "Dual-band terahertz metamaterial absorber and its refractive-index-sensing application for material films," ACS Appl. Opt. Mater. **1**(7), 1281–1288 (2023).
18. D. T. Le, B. T. Tong, T. K. T. Nguyen, *et al.*, "Polarization-insensitive dual-band terahertz metamaterial absorber based on asymmetric arrangement of two rectangular-shaped resonators," Optik **245**, 167669 (2021).
19. H. Soleimani and M. Khorshidi, "Analysis and Equivalent Circuit of Anisotropic Graphene Metasurfaces," Plasmonics **20**(11), 9615–9624 (2025).
20. L. Ju, B. Geng, J. Horng, *et al.*, "Graphene plasmonics for tunable terahertz metamaterials," Nat. Nanotechnol. **6**(10), 630–634 (2011).
21. S. Naghizade, A. Didari-Bader, and H. Saghaei, "Ultra-fast tunable optoelectronic 2-to-4 binary decoder using graphene-coated silica rods in photonic crystal ring resonators," Opt. Quantum Electron. **54**(11), 767 (2022).
22. A. Nayyeri Raad, H. Saghaei, and Y. Safaei Mehrabani, "An optical 2-to-4 decoder based on photonic crystal X-shaped resonators covered by graphene shells," Opt. Quantum Electron. **55**(5), 452 (2023).
23. S. Naghizade and H. Saghaei, "Ultra-fast tunable optoelectronic half adder/subtractor based on photonic crystal ring resonators covered by graphene nanoshells," Opt. Quantum Electron. **53**(7), 380 (2021).
24. B. X. Wang, C. Xu, G. Duan, *et al.*, "Review of broadband metamaterial absorbers: from principles, design strategies, and tunable properties to functional applications," Adv. Funct. Mater. **33**(14), 2213818 (2023).

Optics EXPRESS

25. G. Peng, P. X. Ke, L. C. Tseng, *et al.*, "The design of a multilayer and planar metamaterial with the multi-functions of a high-absorptivity and ultra-broadband absorber and a narrowband sensor," Photonics **10**(7), 804 (2023).
26. M. Fu, N. Xia, Y. Duan, *et al.*, "Tunable broadband terahertz absorber based on graphene with bilayer hexagonal," AIP Adv. **14**(2), 2 (2024).
27. O. M. Daraei, K. Goudarzi, and M. Bemani, "A tunable ultra-broadband terahertz absorber based on two layers of graphene ribbons," Opt. Laser Technol. **122**, 105853 (2020).
28. G. Wu, C. Li, D. Wang, *et al.*, "Terahertz absorber with switchable functionality from ultra-broadband to broadband," Diamond Relat. Mater. **139**, 110306 (2023).
29. Y. Cai and K. D. Xu, "Tunable broadband terahertz absorber based on multilayer graphene-sandwiched plasmonic structure," Opt. Express **26**(24), 31693–31705 (2018).
30. L. Liu, W. Liu, and Z. Song, "Ultra-broadband terahertz absorber based on a multilayer graphene metamaterial," J. Appl. Phys. **128**(9), 9 (2020).
31. M. Nejat and N. Nozhat, "Design, theory, and circuit model of wideband, tunable and polarization-insensitive terahertz absorber based on graphene," IEEE Trans. Nanotechnol. **18**, 684–690 (2019).
32. M. Khorshidi, S. Daghighazar, and R. Ghazizadeh, "A rigorous analytical model and design framework for broadband graphene based THz absorbers," Sci. Rep. **16**(1), 28786 (2026).
33. S. Naghizade, A. Didari-Bader, H. Saghaei, *et al.*, "An electro-optic comparator based on photonic crystal ring resonators covered by graphene nanoshells," Optik **283**, 170898 (2023).
34. S. Naghizade and H. Saghaei, "Tunable electro-optic analog-to-digital converter using graphene nanoshells in photonic crystal ring resonators," J. Opt. Soc. Am. B **38**(7), 2127–2134 (2021).
35. Z. Wang, M. Zhou, X. Lin, *et al.*, "A circuit method to integrate metamaterial and graphene in absorber design," Opt. Commun. **329**, 76–80 (2014).
36. A. Khavasi and B. Rejaei, "Analytical modeling of graphene ribbons as optical circuit elements," IEEE J. Quantum Electron. **50**(6), 397–403 (2014).
37. A. Khavasi, "Design of ultra-broadband graphene absorber using circuit theory," J. Opt. Soc. Am. B **32**(9), 1941–1946 (2015).
38. A. Andryieuski and A. Lavrinenko, "Graphene metamaterials based tunable terahertz absorber: Effective surface conductivity approach," Opt. Express **21**(7), 9144–9155 (2013).
39. S. Atakaramians, V. S. Afshar, T. M. Monro, *et al.*, "Terahertz dielectric waveguides," Adv. Opt. Photonics **5**(2), 169–215 (2013).
40. Y. Yin, Z. Cheng, L. Wang, *et al.*, "Graphene, a material for high temperature devices–intrinsic carrier density, carrier drift velocity and lattice energy," Sci. Rep. **4**(1), 5758 (2014).
41. Y. D. Kim, H. Kim, Y. Cho, *et al.*, "Bright visible light emission from graphene," Nat. Nanotechnol. **10**(8), 676 (2015).
42. H. A. Hafez, S. Kovalev, J. C. Deinert, *et al.*, "Extremely efficient terahertz high-harmonic generation in graphene by hot Dirac fermions," Nature **561**(7724), 507–511 (2018).
43. P. A. D. Gonçalves, "Plasmonics and Light–Matter Interactions in Two-Dimensional Materials and in Metal Nanostructures: Classical and Quantum Considerations," (Springer Nature, 2020).
44. M. Jablan, H. Buljan, and M. Soljačić, "Plasmonics in graphene at infrared frequencies," Phys. Rev. B **80**(24), 245435 (2009).
45. Y. Zhang, T. Li, Q. Chen, *et al.*, "Independently tunable dual-band perfect absorber based on graphene at mid-infrared frequencies," Sci. Rep. **5**(1), 18463 (2016).
46. C. Zhang, C. Tang, and J. Sun, "Graphene-based dual-broadband terahertz absorber with independent frequency and amplitude tunability," AIP Adv. **14**(10), 10 (2024).
47. R. Misra, M. McCarthy, and A. F. Hebard, "Electric field gating with ionic liquids," Appl. Phys. Lett. **90**(5), 052905 (2007).
48. E. Piatti, L. Guglielmero, G. Tofani, *et al.*, "Ionic liquids for electrochemical applications: Correlation between molecular structure and electrochemical stability window," Journal of Molecular Liquids **364**, 120001 (2022).
49. Y. Wu, X. Qiu, H. Liu, *et al.*, "Tunable terahertz reflection of graphene via ionic liquid gating," Nanotechnology **28**(9), 095201 (2017).
50. L. Ye, X. Chen, G. Cai, *et al.*, "Electrically tunable broadband terahertz absorption with hybrid-patterned graphene metasurfaces," Nanomaterials **8**(8), 562 (2018).
51. S. Biabanifard, M. Biabanifard, S. Asgari, *et al.*, "Tunable ultra-wideband terahertz absorber based on graphene disks and ribbons," Opt. Commun. **427**, 418 (2018).
52. J. Qian, J. Zhou, Z. Zhu, *et al.*, "Polarization-insensitive broadband THz absorber based on circular graphene patches," Nanomaterials **11**(10), 2709 (2021).
53. M. Fu, N. Xia, Y. Niu, *et al.*, "Tunable wideband terahertz absorber based on single-layer patterned graphene," Opt. Commun. **570**, 130843 (2024).
54. R. Zheng, Y. Liu, L. Ling, *et al.*, "Ultra wideband tunable terahertz metamaterial absorber based on single-layer graphene strip," Diamond Relat. Mater. **141**, 110713 (2024).
55. S. Jorwal, A. Dubey, R. Gupta, *et al.*, "A tunable, dual band graphene terahertz absorber with equivalent circuit modeling," Opt. Quantum Electron. **56**(8), 1377 (2024).
56. Y. F. C. Chau, "Enhancing broadband terahertz absorption via a graphene-based metasurface absorber featuring a rectangular ring and triple crossbars," Phys. Scr. **99**(5), 055905 (2024).
57. O. M. Daraei, P. Rezaei, P. Zamzam, *et al.*, "Single/multi-band graphene-based disk THz absorbers with single graphene layer: Conceptual design," Opt. Quantum Electron. **56**(11), 1844 (2024).
58. P. Upender and K. Yadav, "Tunable terahertz biosensing and shielding using a graphene-enhanced dielectric resonator absorber," Sci. Rep. **15**(1), 26352 (2025).